Mon. Not. R. Astron. Soc. **000**, 1–17 (2010) Printed 8 March 2011 (MN LaTeX style file v2.2)

arXiv:1009.5519v2 [astro-ph.CO] 7 Mar 2011

Expected properties of the Two-Point Autocorrelation Function of the IGM

Ursino, E.[1]*, Branchini, E.[1], Galeazzi, M.[2], Marulli, F.[3], Moscardini, L.[3,4], Piro, L.[5], Roncarelli, M.[6], and Takei, Y.[7]

[1] *Dipartimento di Fisica, Universitá di Roma TRE, Via della Vasca Navale 84, I-00146, Roma, Italy*
[2] *Physics Department, University of Miami, Coral Gables, FL 33155*
[3] *Dipartimento di Astronomia, Universitá degli Studi di Bologna, Via Ranzani 1, I-40127, Bologna, Italy*
[4] *INFN, Sezione di Bologna, viale Berti Pichat 6/2, I-40127 Bologna, Italy*
[5] *INAF-Istituto di Astrofisica Spaziale Fisica Cosmica, Via del Fosso del Cavaliere 100, I-00133 Roma, Italy*
[6] *Centre d'Etude Spatiale des Rayonnements (CESR), 9, av. du Colonel Roche - B.P. 44346, 31028, Toulouse Cedex 4, France*
[7] *Institute of Space and Astronautical Science (ISAS), JAXA, 3-1-1 Yoshinodai, Chuo-ku, Sagamihara, Kanagawa 252-5210 Japan*

Accepted . Received ;

ABSTRACT

Recent analyses of the fluctuations of the soft Diffuse X-ray Background (DXB) have provided indirect detection of a component consistent with the elusive Warm Hot Intergalactic Medium (WHIM). In this work we use theoretical predictions obtained from hydrodynamical simulations to investigate the angular correlation properties of the WHIM in emission and assess the possibility of indirect detection with next-generation X-ray missions. Our results indicate that the angular correlation signal of the WHIM is generally weak but dominates the angular correlation function of the DXB outside virialized regions. Its indirect detection is possible but requires rather long exposure times [0.1-1] Ms, large ($\sim 1^\circ \times 1^\circ$) fields of view and accurate subtraction of isotropic fore/background contributions, mostly contributed by Galactic emission. The angular correlation function of the WHIM, which turns out to be positive for $\theta < 5'$ provides limited information on its spatial distribution. A satisfactory characterization of the WHIM in 3D can be obtained through spatially resolved spectroscopy. 1 Ms long exposures with next generation detectors will allow to detect ~ 400 O VII+O VIII X-ray emission systems that could be used to trace the spatial distribution of the WHIM. We predict that these observations will allow to estimate the WHIM correlation function with high statistical significance out to ~ 10 Mpc h^{-1} and characterize its dynamical state through the analysis of redshift-space distortions. The detectable WHIM, which is typically associated with the outskirts of virialized regions rather than the filaments has a non-zero correlation function with slope $\gamma = -1.7 \pm 0.1$ and correlation length $r_0 = 4.0 \pm 0.1$ Mpc h^{-1} in the range $r = [4.5, 12]$ Mpc h^{-1}. Redshift space distances can be measured to assess the dynamical properties of the gas, that we predict to be typically infalling onto large virialized structures.

Key words: diffuse radiation – large-scale structure of universe (WHIM) – X-rays: diffuse background

1 INTRODUCTION

The observed abundance of baryons in the local Universe does not agree with the high redshift observations (Fukugita, Hogan, & Peebles 1998). The Lyman alpha forest at $z = 2$, the results from the WMAP experiment, and the predictions of the standard nucleosynthesis model are all consistent with a baryonic density $\Omega_B \simeq 0.04$ (Rauch et al. 1998; Weinberg et al. 1997; Burles & Tytler 1998; Kirkman et al. 2003; Bennett et al. 2003; Spergel et al. 2007; Komatsu et al. 2009). At variance with these results, the baryon mass in stars, galaxies, and clusters in the local Universe seems to be $2 - 4$ times lower.

Large-scale cosmological hydrodynamic simulations (Cen & Ostriker 1999a; Croft et al. 2001; Yoshikawa et al. 2003; Chen et al. 2003; Borgani et al. 2004; Cen & Ostriker

---

* E-mail: ursino@fis.uniroma3.it

2006; Shen, Wadsley, & Stinson 2010; Smith et al. 2010; Tornatore et al. 2010) allow to follow the evolution of baryons from high redshift to present days. A common feature of these simulations is that $40-50$ % of the baryons in the Universe at $z \sim 0$ are in the form of highly ionized gas with temperature in the range of $10^5 - 10^7$ K. This gas is characterized by a spatial distribution that closely resembles that of the underlying cosmic web of the Dark Matter, and is commonly indicated as the Warm-Hot Intergalactic Medium (WHIM). According to thermal emission models for gas in collisional equilibrium (Raymond & Smith 1977) and assuming an average metallicity of 0.1 $Z_\odot$, this highly ionized gas emits mainly in the soft X-ray ([0.1-1] keV) and in the Far and Extreme UltraViolet (FUV, [0.01-0.1] keV) energy bands. However, the expected WHIM contribution to the total surface brightness (SB) in these bands is expected to be weak. The comparison between the predicted emission of the WHIM and the measured Diffuse X-Ray Background (DXB), for example, shows that the WHIM contribution to the total SB is in the order of 10% (Phillips, Cen, & Ostriker 2001; Ursino & Galeazzi 2006; Ursino, Roncarelli, & Galeazzi 2010). Highly ionized metals in the warm-hot gas are responsible for line emission or absorption features whose strength is also expected to be rather weak (Kravtsov, Klypin, & Hoffman 2002; Chen et al. 2003; Klypin et al. 2003; Viel et al. 2003; Yoshikawa et al. 2003, 2004; Cen & Fang 2006; Branchini et al. 2009).

Observational data confirm the difficulty to detect WHIM lines, both in absorption and emission. A clear detection of the WHIM comes from the absorption lines of ions like O vi, N v, C iii, C iv, Si iii, Si iv, and Fe iii in the FUV spectra of bright, distant sources. Roughly a hundred FUV absorbers have been detected in the spectra of $\sim$ 30 AGN (Danforth & Shull 2005, 2008; Thom & Chen 2008; Tripp et al. 2008). Their abundance turned out to be in agreement with theoretical predictions (Cen & Fang 2006). However, these absorbers trace only the warm gas (T$<$ 10^6 K) whereas the bulk of the WHIM is expected to be at higher temperatures. In the soft X-ray band the search for the WHIM has led to a few detections (Fang et al. 2002; Nicastro et al. 2005; Fang, Canizares, & Yao 2007; Buote et al. 2009; Fang et al. 2010; Williams et al. 2010) whose statistical significance is still under debate (Kaastra et al. 2006; Rasmussen et al. 2007). In emission, the only claim for a line detection so far is likely to be associated with a gas filament connecting the two galaxy clusters A222 and A223 (Werner et al. 2008). However, the overdensity ($\delta \simeq 150$) and the temperature (T$\sim 1 \times 10^7$ K) of this gas are only marginally consistent with the WHIM definition. In addition, Zappacosta et al. (2002); Mannucci et al. (2007) observed a soft X-ray excess associated to galaxy concentration and possibly consistent with WHIM emission.

Finally, an indirect evidence for the WHIM comes from the analysis of the Diffuse DXB in the soft band [0.4-1.0] keV, which is known to be mainly contributed by unresolved AGN, starburst galaxies and local diffuse emission (Snowden et al. 1997; Mushotzky et al. 2000; McCammon et al. 2002; Galeazzi et al. 2007; Henley & Shelton 2008; Gupta & Galeazzi 2009; Henley & Shelton 2010). These sources account for all but 10% to 20% of the DXB (Hickox & Markevitch 2007) matching the theoretical expectations for the WHIM emission in this band (Roncarelli et al. 2006).

The WHIM is also expected to provide some contribution, perhaps with characteristic features, to the angular correlation properties of the DXB fluctuations. Such contribution, if detected, would provide a further, indirect evidence for the WHIM. Indeed, a recent angular correlation analysis of the unresolved DXB measured by *XMM* (Galeazzi, Gupta, & Ursino 2009) has revealed the presence of a component that has been identified with the WHIM. Future X-ray missions are expected to detect a large number of characteristic emission lines in the X-ray band through which one will be able to unambiguously detect the WHIM (Cen & Fang 2006) and probe its spatial distribution much more densely than it could be possibly done in absorption, due to the paucity of the background sources (Viel et al. 2003, 2005). Therefore one expects that only emission studies in the X-ray band will be able not only to detect the WHIM and characterize its thermal state, but also to provide a tomography of a large fraction of the missing baryons in the local universe. In particular, as we will show in this work, given the characteristic of next-generation X-ray detectors, the estimate of the spatial two-point correlation function of the WHIM line-emitting regions will allow to characterize the spatial correlation properties of the WHIM and its dynamical state.

In this work we investigate the possibility of characterizing the angular and spatial distribution of the WHIM using next-generation X-ray satellites. More specifically, we aim at two different but related goals. First we investigate the possibility of finding the signature of the WHIM in the angular correlation function of the unresolved DXB. Second, we assess the possibility of tracing the spatial distribution and the dynamical state of the WHIM by detecting its characteristic emission lines and measuring the spatial two-point correlation function of the line-emitting regions. The two ingredients required for this goal are: a theoretical WHIM model to rely upon and a reference experimental setup. For the WHIM model we assume the same one as of Ursino et al. (2010) and Branchini et al. (2009), based on the Borgani et al. (2004) hydrodynamical simulation. As a reference experimental setup we consider the recently proposed *Xenia* [1] X-ray satellite (Hartmann et al. 2009). The reason for considering this particular mission is that it is designed to carry two instruments well suited for our purposes: the High Angular Resolution Imager (HARI) and the Cryogenic Imaging Spectrometer (CRIS). The HARI is a CCD or CMOS based detector with a field of view (f.o.v) shaped as a circle of diameter 1.4°, angular resolution of $15''$ for on-axis objects, and energy resolution of $50-150$ eV FWHM (in the range $0.3-5.0$ keV). The CRIS is a spatially resolved spectrometer based on Transition Edge Sensor technology. The imaging area is $0.9^\circ \times 0.9^\circ$, angular resolution is $\sim 2.5'$, and the energy resolution is in the range [1-3] eV. The X-ray telescope has an effective area of 1000 cm^2 at 1 keV. The HARI instrument is expected to provide the possibility to study the angular correlation properties of the DXB and isolate the WHIM contribution thank to its large f.o.v. and angular resolution, smaller than the typical angular size of the WHIM emitting element (Ursino & Galeazzi 2006). The CRIS instrument will allow to detect the WHIM emission lines and identify the spatial position of the emitting gas thanks to the good angular and energy resolution.

---

[1] http://sms.msfc.nasa.gov/xenia/

The plan of the paper is as follows. In Section 2 we introduce the WHIM model and the procedure we adopted to generate the simulated X-ray maps and spectra that will be considered for the correlation analysis. In Section 3 we describe the estimator used to compute the angular two-point correlation function and estimate the contribution of the WHIM to the DXB angular correlation signal in the case of a simulated observation with *Xenia* . In Section 4 we measure the spatial two-point correlation function in the simulated maps and assess the possibility of characterizing the spatial distribution and dynamical state of the WHIM in the case of a *Xenia* observation.In Section 5 we summarize and discuss the results of our work.

2 SIMULATED DATASETS

In this section we briefly describe the hydrodynamical simulation of Borgani et al. (2004), the WHIM model built upon these (Ursino et al. 2010; Branchini et al. 2009) and the mock X-ray SB maps and spectra obtained from this model taking into account the response functions of the HARI and CRIS detectors.

2.1 The Hydrodynamical Model of the WHIM

The WHIM model considered in this work has been obtained from the hydrodynamical simulation of Borgani et al. (2004). This simulation assumes a flat ($\Omega_m = 0.3$, $\Omega_\Lambda = 0.7$) ΛCDM model with a nonvanishing cosmological constant, with $h = 0.7$, $\Omega_b = 0.04$, and $\sigma_8 = 0.8$. The simulation was performed using the TREESPH code GADGET-2 (Springel, White, & Hernquist 2001; Springel 2005) with a Plummer equivalent softening, fixed in comoving units, $\epsilon_{Pl} = 7.5\ h^{-1}\ kpc$ at $z < 2$, and fixed in physical units at $z > 2$. The simulation follows the evolution of 480^3 dark matter (DM) particles and 480^3 baryonic gas particles from redshift $z = 49$ to $z = 0$. The simulation box has a side of 192 h^{-1} Mpc. DM and gas particles have masses $m_{DM} = 4.62 \times 10^9\ h^{-1}\mathrm{M}_\odot$ and $m_{gas} = 6.93 \times 10^8\ h^{-1}\mathrm{M}_\odot$, respectively. Radiative cooling was performed under the assumption of optically thin gas with pristine composition (76% hydrogen and 24% helium) and in collisional equilibrium. The simulation includes a time-dependent photoionizing UV background that reionizes the Universe at $z \simeq 6$ (Haardt & Madau 1996). A two-phase model (Springel & Hernquist 2003) and a Salpeter initial mass function (Salpeter 1955) were assumed in the simplified star formation model. Galactic winds with typical velocity of about 350 km s^{-1} were assumed to carry energy, mass, and metals produced by stars in the IGM (Springel & Hernquist 2003). The simulation output consists of 102 boxes, equally spaced in logarithmic redshift scale between $z = 9$ and $z = 0$. This simulation correctly reproduces the observational properties of rich X-ray emitting clusters (Borgani et al. 2004) but overestimates the emission from smaller structures that can be identified with galaxy groups. This overestimate probably originates from having assumed primordial composition in the cooling function, instead of updating the cooling rate according to the evolving metallicity of the gas (Bertone et al. 2010). However, this effect is not expected to affect significantly the emission properties of the WHIM gas in regions of lower density, outside virialized structures, characterized by an average metallicity well below solar (Shen et al. 2010) The fact that our WHIM model does not exceed the DXB constraint (Roncarelli et al. 2006) corroborates this assumption. In fact, the overestimate of the X-ray emission from galaxy groups artificially reduces the contribution of the WHIM to the DXB. In this respect, all theoretical prediction on the WHIM detectability presented in this work are to be regarded as conservative.

Metal diffusion is described by particles that actually undergo metal enrichment by star formation, and not by transfer of metals between neighboring particles (Wiersma, Schaye, & Smith 2009). As a result, the spatial distribution of metals may result unrealistically inhomogeneous, in particular for the gas in lower density regions (like the WHIM), far away from star forming regions. To circumvent this potential problem, we did not use the metallicity calculated self-consistently within the simulation. Instead, we assigned a metallicity to all gas particle in each simulation output by matching the metallicity-density relation in the simulation of Cen & Ostriker (1999b). In practice, at a given output, we consider each gas particle with density ρ, and assign a gas metallicity according to the probability function $P(Z(\rho, z))$ built upon the simulation outputs of Cen & Ostriker (1999a), as fully described in Ursino et al. (2010). It is reassuring that, with this metallicity prescription, the WHIM model correctly reproduces the observed abundances of O VI absorbers and satisfies the current constraints for the O VII lines (Branchini et al. 2009).

Since we are interested in modeling X-ray observations of the WHIM, we focused our analysis on gas at temperatures higher than 10^5 K. We adopted the definition of the WHIM as the gas with $10^5 < \mathrm{T} < 10^7$ K and $\rho \leqslant 1000\langle\rho\rangle$, distributed along a network of filaments connecting virialized structures and in their outskirts. For the purpose of characterizing the angular and spatial correlation properties of the WHIM, however, we find it more convenient to consider different classifications for the gas phases that we describe here for reference.

In § 3, to study the angular correlation properties of the DXB, we find it more convenient to divide the gas into three phases:

- The WHIM, which coincides with the previous definition.
- The *non*-WHIM.
- The *Total Gas*, which represents the sum of the two contributions, i.e. all gas with $\mathrm{T} > 10^5$ K.

In § 4, to study the spatial correlation properties of the line-emitting gas, we consider the following phases:

- The *Total Gas*, the gas responsible for detectable line emission, irrespective of its thermal state or number density.
- The *Bright*-WHIM represents gas regions in which the WHIM contributes to the emission of detectable X-ray lines (i.e. regions where the WHIM contribution is above the detectability threshold, described in § 2.3), regardless whether

the non-WHIM contribution is stronger of the WHIM contribution or not, or whether the non-WHIM contribution is above the detectability threshold.

- The WHIM-*dominated* gas, represents gas regions in which the WHIM contribution to the line emission is larger than that of all other phases and the sum of the WHIM and non-WHIM contributions is above the detection threshold, even though the WHIM contribution alone is not above the detection threshold.

The *Total Gas* traces dense and bright regions (usually groups and clusters), as well as the less dense regions where the WHIM resides (outskirts and bright filaments). The *Bright*-WHIM gas could trace also the brightest regions if, model-wise, they are multiphase and have a WHIM contribution above detectability. The WHIM-*dominated* gas traces only the bright filaments and the outskirts of virialized structures, while in the cores of virialized structures the WHIM contributes to emission less than the hot and dense gas.

2.2 Mock X-Ray emission maps

To study the angular correlation properties of the WHIM and assess the possibility of its indirect detection we have generated a suite of mock SB maps in the soft X-ray band. Here we summarize the procedure to generate the maps and refer the interested reader to Ursino et al. (2010) for a more detailed description. As a first step we consider all gas particles within a light-cone, extracted from the hydrodynamical simulation. The light-cone is obtained by stacking the simulation output at different epochs out to $z = 2$ (Roncarelli et al. 2006). X-ray maps are obtained by considering the individual contribution of all the particles within the light-cone to the SB. In particular, for every particle we obtain the X-ray spectrum from the APEC model of the XSPEC [2] package to simulate the emission from the plasma. Spectra are fully specified by the temperature, density, and metallicity of the particle. Here we focus on the energy range 0.380−0.650 keV, where the WHIM contribution to the DXB is thought to be maximum. The lower limit of 0.38 keV allows us to exclude the strong local C VI line (0.367 keV) that would superimpose and dominate the weaker redshifted O VII and O VIII lines. The upper limit allows us to include the O VII triplet and the O VIII line at redshift zero, as well as redshifted lines of heavier metals like Fe XVII (0.826 keV), Ne IX (0.922 keV), and Mg XI (1.352 keV). The use of the APEC model is justified under the assumption that the gas is in collisional equilibrium. The goodness of this hypothesis is guaranteed by the fact that emission is proportional to the square of density. This is also valid for the WHIM contribution which, therefore, mostly comes from high density regions in which the gas is usually hotter and the ionization balance is set by collisions only.

To account for the angular resolution of the detector we have binned the particles' contributions to the flux into square pixels. The flux in each pixel account for the contribution from all particles within the pixel itself plus that of particles in neighboring pixels weighted according to their smoothing kernel. All maps account for the effect of absorption due to the neutral hydrogen in our Galaxy. We modeled absorption according to Morrison & McCammon (1983), applying a typical value at high latitude of $N_H = 1.8 \times 10^{20}$ cm^{-2} (McCammon et al. 2002). Overall we have generated 10 simulated maps of the DXB in the energy range 380 − 650 eV. We have binned the 1° × 1° f.o.v with 256 × 256 pixels in order to obtain an angular resolution of $14'' \times 14''$ comparable to that expected for the HARI instrument. These maps constitute the database that we will analyze in § 3.

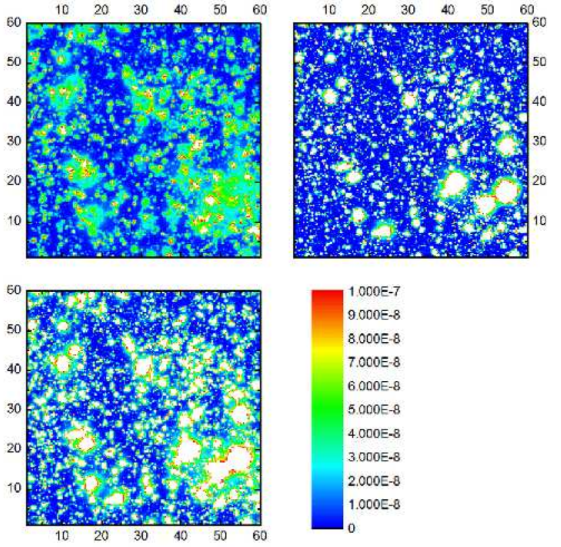

Figure 1. Mock Surface brightness in the 380 − 650 eV energy band, f.o.v. of 1° × 1° and angular resolution $14'' \times 14''$. Contributions from the WHIM (*top-left*) and *non*-WHIM (*top-right*) phases are shown together with the *Total Gas* signal (*bottom-left*). Color scale indicates different SB levels in units of photon cm^{-2} s^{-1}.

Fig. 1 shows a typical mock SB map with a f.o.v. of 1° × 1° and angular resolution of $14'' \times 14''$. The bottom panel shows the flux in the 0.380 − 0.650 keV band contributed by all gas particles with $T > 10^5$ K (i.e. the *Total gas*). The top-left and top-right panels show the contribution of the WHIM and *non*-WHIM phases, respectively. These mock maps also include an isotropic signal contributed by a a Galactic foreground (McCammon et al. 2002) and a diffuse extragalactic background of unresolved AGN, that we describe in details in § 3.3.

In Tab. 1 we have listed the mean SB contributed by the various components: WHIM, *non*-WHIM, Galactic foreground and unresolved AGN. While, as already pointed out, the WHIM contribution is consistent with observational constraints, the *non*-WHIM component exceeds these limits (Borgani et al. 2004). To quantify the mismatch is convenient to refer to the 0.65 − 1 keV band in which observational constraints have been derived by Hickox & Markevitch (2007). The observational value of $(1.0 \pm 0.2) \times 10^{-12}$ ergs cm^{-2} s^{-1} deg^{-2} is reassuringly larger than the expected WHIM contribution of $(3.6 \pm 0.3) \times 10^{-13}$ ergs cm^{-2} s^{-1} deg^{-2}. On the contrary the *non*-WHIM contribution of $(8.7 \pm 0.5) \times 10^{-12}$ ergs cm^{-2} s^{-1} deg^{-2}

---

[2] http://heasarc.gsfc.nasa.gov/docs/xanadu/xspec/

Table 1. Contributions to the DXB from the different gas phases in the $380 - 650$ eV energy band.

	photon $\mathrm{cm^{-2}\ s^{-1}\ deg^{-2}}$
WHIM^a	$(1.6 \pm 0.2) \times 10^{-3}$
non-WHIM^a	$(8.9 \pm 1.1) \times 10^{-3}$
Galactic Foreground^b	$(3.39 \pm 2.26) \times 10^{-3}$
AGN^c	$(0.53 \pm 0.03) \times 10^{-3}$

[a] Mean values and standard deviations calculated from 10 maps.
[b] Model by McCammon et al. (2002), cosmic variance estimated from Gupta et al. (2009); Henley & Shelton (2010).
[c] Double power-law model (see section 3.3.3), errors extrapolated from Moretti et al. (2003).

largely exceeds the observational constraints as a result of the fact that the simulation overestimates the X-ray luminosity associated to galaxy groups, as anticipated in the previous section.

2.3 Mock 2D spectra

To study the spatial correlation properties of the WHIM we have simulated data cubes representing a 2D-spectrum similar to that that will be taken by a spectrograph like CRIS. For this purpose we have used our WHIM model to obtain a "map" consisting of a collection of 1D-spectra from contiguous pixels across a $5.5° \times 5.5°$ area. Here we just summarize the main step of the procedure used to generate these mock spectra and refer the interested reader to Takei et al. (2010) for a more detailed description. The possibility of performing a 3D correlation analysis of the WHIM relies on the possibility of detecting its characteristic X-ray emission lines. Detection estimates using our model have been obtained by Takei et al. (2010) and will be adopted here.

To produce the spectra we adopt a procedure similar to that of the mock SB maps except that here we consider larger pixels ($\sim 1.3' \times 1.3'$ corresponding to $\sim 50\%$ of the CRIS angular resolution) and wider f.o.v. ($5.5° \times 5.5°$, roughly corresponding to a mosaic of 25 CRIS pointings). The result is a collection of 256×256 mock 1D-spectra, one for each pixel. Furthermore, to account for the energy resolution of the instrument, we divide the particle distribution along each angular resolution element into radial bins of comoving length 3 Mpc $\mathrm{h^{-1}}$ (approximately corresponding to $\Delta E \sim 1$ eV). We end up with $256 \times 256 \times 448 \simeq 3 \times 10^7$ mock resolution elements containing spectra convolved with the response matrix of the instrument that include the effect of Galactic absorption, modeled as in Morrison & McCammon (1983), with a column density of $1.8 \times 10^{20}\ \mathrm{cm^{-2}}$ (McCammon et al. 2002).

To reduce the CPU time and memory requirement we have considered only gas particles out to $z = 0.5$, corresponding to a maximum comoving depth of our correlation analysis of ~ 1344 Mpc $\mathrm{h^{-1}}$. In addition, since we are interested in the O VII and O VIII lines only, spectra in each bin have been generated using only particles that provide contribution in the narrow energy range corresponding to that of the two redshifted lines.

To perform the 3D correlation analysis we consider only those resolution elements in which the surface brightness of the O VIII line is above 7×10^{-2} photon $\mathrm{cm^{-2}\ s^{-1}\ sr^{-1}}$, a threshold that guarantees a 5-σ detection in a 1 Ms observation with the CRIS instrument (Takei et al. 2010). We consider the O VIII line only, rather than the simultaneous detection of O VII and O VIII. This choice is justified by the fact that $\sim 90\%$ of O VIII brighter than our selection threshold is associated to a detectable O VII line, as shown by Takei et al. (2010) (Table 1 Model B2, $t_{exp} = 1$ Ms). The visual inspection of the 3D maps corroborates the remarkable spatial coincidence between the O VII+O VIII and the O VIII-only line-emitting regions (Takei et al. 2010).

In the geometry of our problem, the comoving volume of the resolution element increases with redshift. Since the typical size of line-emitting regions is not expected to evolve significantly out to $z = 0.5$, the risk is of over- or under-sampling a line-emitting region, depending on its redshift. To circumvent the problem we have grouped the spatially-contiguous resolution elements with detectable O VIII lines into a single object, which we call *emitter*, and study the correlation of such emitters. To assess the robustness of our results with respect to the grouping scheme, we have implemented two different grouping procedures. In the first, we link all resolution elements having one side in common. In the second, we group the elements that have one edge or one vertex in common. We have verified that using either schemes does not significantly modify the results and therefore we will only discuss the results obtained with the first, more conservative, grouping scheme. The outcome of the grouping procedure is a list of O VIII emitters characterized by their total O VIII line surface (obtained by summing over the grouped elements) and spatial position (defined as the SB-weighted centre of mass of the emitter). As a final remark, we note that the 3 Mpc $\mathrm{h^{-1}}$ binning introduces a spurious periodicity along the line of sight which we eliminate by randomizing the position of the emitter along the line of sight, within the resolution element.

3 ANGULAR CORRELATION ANALYSIS OF THE WHIM

In this section we address the problem of detecting the WHIM signature in the angular correlation signal of the DXB. We first describe the statistical tool used for the analysis, i.e. the two-point correlation function, then we apply it to the ideal case of an arbitrarily long exposure time and no contribution from AGN and Galactic foreground. Then we include all contaminations to simulate a realistic observational setup.

3.1 The angular correlation function

As shown in Tab. 1, the Galactic foreground and the *non*-WHIM gas dominate the mean DXB signal in the $380 - 650$ eV energy range. The component we are interested in, the WHIM, is largely subdominant (less than 10%) but its spatial distribution, from hydro simulations, is markedly different from that of the other components. Under such circumstances, which are reminiscent to that of the CMB signal, the best option to infer the presence of the WHIM is by analyzing the two-point angular correlation function (ACF) of the DXB.

We characterize the angular correlation properties of the DXB by measuring the angular two-point correlation function $w(\theta)$ of the signal in the mock maps. To measure $w(\theta)$ we use the Landy-Szalay estimator (Landy & Szalay 1993) [LS from now on]:

$$1 + \hat{w}(\theta) = \frac{DD - 2DR + RR}{RR}, \tag{1}$$

where θ is the angle between two pixels in the map and

$$DD(\theta) = \frac{\sum g_{ij} g_{kl}}{(\sum g_{ij})^2}, \tag{2}$$

$$DR(\theta) = \frac{\sum g_{ij} r_{kl}}{\sum g_{ij} \sum r_{kl}}, \tag{3}$$

$$RR(\theta) = \frac{\sum r_{ij} r_{kl}}{(\sum r_{ij})^2}. \tag{4}$$

DD represents the number of photon pairs, normalized to the total counts, obtained by summing over all photon counts g_{ij} in two pixels i and j separated by θ. RR is the analogous quantity for a map in which the photons are uniformly distributed across the f.o.v (the Random sample). DR represents the mixed counts contributed by pixels in the real and random dataset. We have verified that the LS estimator is equivalent to that used by other authors (Ursino & Galeazzi 2006; Galeazzi et al. 2009).

In this work we estimate the ACF of the DXB, the ACFs of its components and their cross-terms. For the simple case in which the DXB is the sum of two components, A and B, with ACF ω_A and ω_B respectively, the following relation holds for the ACF of the DXB;

$$n_T^2 w_T(\theta) = n_A^2 w_A(\theta) + n_B^2 w_B(\theta) + 2\, n_A n_B w_{AB}(\theta), \tag{5}$$

where n_A and n_B are the photon counts contributed by the two components, $n_T = n_A + n_B$, and ω_{AB} is the cross-correlation term.

Uncertainties in the ACF are estimated as the RMS scatter among the correlation functions measured among the ten, statistically independent, mock maps .

3.2 Ideal Case

Are the angular correlation properties of the WHIM significantly different from those of the other components? We address this question by computing the ACF in the ideal case of an arbitrarily long observation with the HARI instrument, ignoring all additional components like the Galactic foreground (which is assumed to be perfectly subtracted) and unresolved sources like AGN (that are assumed to provide a negligible contribution, as we will show in Section 3.3.3).

For the purpose of detecting the WHIM signature, it is useful to compare the ACF of the flux map of the WHIM and *non*-WHIM components. Fig. 2 compares the ACF of the WHIM (red, dashed line) with that of the *non*-WHIM (dotted, green). Lines represent the mean ACFs of the ten mock mapsvvand the band their rms scatter. As expected, the *non*-WHIM provides the dominant contribution to the total signal (solid, black line). Even the cross-correlation signal (dot-dashed, blue line), estimated by subtracting the WHIM and *non*-WHIM contributions from the total ACF signal, is higher than that of the WHIM. However the WHIM autocorrelation signal is significantly above zero out to $\theta \simeq 6'$. The fact that the WHIM and *non*-WHIM ACFs have similar shapes is rather disappointing since it means that no characteristic feature in the ACF of the WHIM can be used to unambiguously infer its presence. On the other hand, the small amplitude of the WHIM correlation signal is less of a problem, considering that all ACFs in Fig. 2 are normalized to the total flux. Indeed, the amplitude of the *intrinsic* ACF of the WHIM, i.e. any term $w(\theta)$ in Eq. 5, is similar to that of the *non*-WHIM. The difference in amplitude reflects the different mean flux of the two phases: a suppression factor of $\left(\frac{n_{\rm WHIM}}{n_{non-{\rm WHIM}}}\right)^2 \sim 30$, with $\mathrm{n}_{\rm WHIM}$ and $\mathrm{n}_{non-{\rm WHIM}}$ the WHIM and the *non*-WHIM SB respectively, is expected between the ACF of the WHIM and that of the *non*-WHIM. This is encouraging and suggests that the WHIM correlation signal could be extracted from the total one, provided that the ACF is estimated in regions where the WHIM emission dominates over the *non*-WHIM one. Such regions are clearly seen in Fig. 1 and show that WHIM emission is preferentially located at the outskirts of virialized structures whose central regions are, on the contrary, dominated by the *non*-WHIM component.

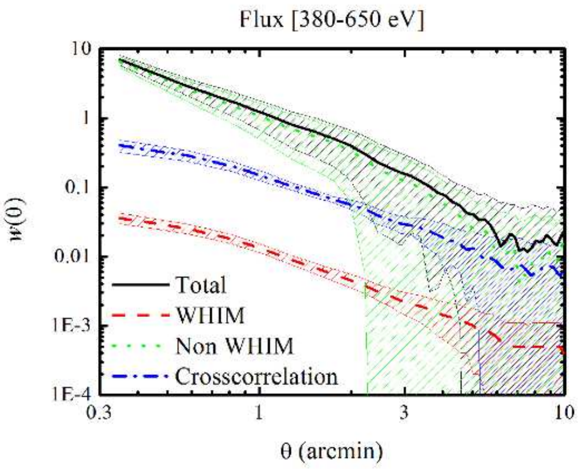

Figure 2. ACFs of the WHIM (*dashed red*), *non*-WHIM (*dotted green*), cross correlation term (*dot-dashed blue*) and their sum (*solid black*). Amplitudes are normalized to the total flux.

These mock maps suggest that a possible strategy to extract the WHIM autocorrelation signal is to exclude from the correlation analysis the pixels associated to the large virialized structures in which the SB is usually larger. To optimize the cleaning procedure one has to compromise between discarding pixels in which the signal is dominated by the *non*-WHIM component, and the need of using as many pixels as possible to increase the statistical significance of the signal. Our mock maps, in which we can pinpoint the contribution of the different components, allow us to calibrate this procedure. We have found that a very simple, yet effective, strategy is to exclude pixels with SB above a fixed threshold.

Fig. 3 shows the result of having restricted the estimate of the ACF to $\sim 50\%$ faintest pixels of the map. The result

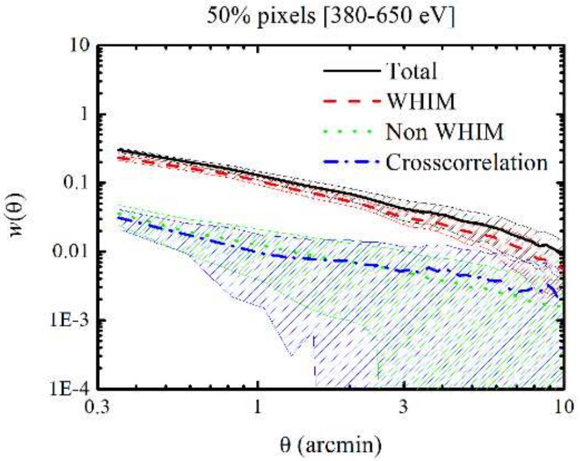

Figure 3. Same as Fig. 2 after removing the brightest 50% pixels from the map.

demonstrates the goodness of our strategy: the ACF signal from the faint regions of the map is indeed dominated by the WHIM emission, as expected, and its ACF can be regarded as an indirect detection of the WHIM even in absence of characteristic signatures in the correlation signal. It is worth stressing that the method of discarding bright pixels is a very rough one and can be easily improved, for example by targeting the pixels associated to known X-ray sources. Yet, given the current uncertainties in the WHIM model and for the purpose of obtaining an order of magnitude estimate on the possibility of extracting the WHIM correlation signal, we do not try to improve the "cleaning" procedure and focus instead on the problem of dealing with observational uncertainties.

3.3 Realistic Case

We now repeat the analysis of § 3.2 using more realistic mock maps which account for instrumental effects (exposure time and collecting area) and for the presence of quasi-isotropic fore/backgrounds (Galactic foreground and unresolved AGN).

3.3.1 Discrete photon counts

In a realistic observational setup with finite exposure time and collecting area, one deals with photon counts. In order to transform the maps of § 3.2 into photon counts maps, we multiply the flux by the exposure time and the effective area of the detector. We consider observations with t_{exp} in the range [0.1-1] Ms and a detector of effective area $A = 10^3$ cm^2, to mimic a long/very long exposure with the HARI ccd.

To generate the discrete photon maps we adopt a four-step procedure. As a first step we compute the total (integer) number of photons in the map as $N_{tot} = int\left(\sum_{ij} f_{ij} A\, t_{exp}\right)$, where f_{ij} is the expected flux in the pixel with coordinates (i, j) and the sum runs over all the pixels. In the second step we assign each pixel the corresponding (integer) number of photons $N_{ij} = int\,(f_{ij} A\, t_{exp})$ and we keep track of the difference $P_{ij} = f_{ij} A\, t_{exp} - N_{ij} \in [0, 1)$. In the third step, we assign the remaining $N_{tot} - \sum_{ij} N_{ij}$ photons through Monte Carlo rejection procedure that randomly assigns photons to pixels with probability $P(i, j)$. Finally, we set the ratio of WHIM/*non*-WHIM photons equal to that of the WHIM/*non*-WHIM fluxes.

We did not add Poisson noise to the photon count maps since, for long exposure times, the error budget is dominated by field-to-field variance rather than shot noise. To justify this hypothesis we have evaluated the expected Poisson error using the following theoretical expression (Cabrè & Gaztañaga 2009):

$$\Delta\xi(r) = \sqrt{\frac{(N_R/N_D)^2 + 4(N_R/N_D)}{RR(r)}}, \tag{6}$$

where N_R and N_D represent the number of emitters in the real and random catalog. In our case we have used $N_R = N_D$.

Here we focus on the WHIM signal in the maps from which we have removed the 50% brightest pixels. In this case we find that field-to-field variance dominates the error budget for $t_{exp} \sim 1$ Ms. As a result, the ACFs and its errors computed from the photon maps are identical to those computed from the flux maps, in the ideal case (e.g. Fig. 2). However, when $t_{exp} \sim 100$ ks the Poisson noise contribution is no more negligible and accounts for $\sim 50\%$ of the error budget. To account for this effect we have increased the error bars on the corresponding maps by a factor $\sqrt{2}$. Instead, when we consider the *Total gas* signal in the original maps (i.e. with no bright pixel removal) the Poisson noise is largely subdominant, even for exposure times as short as 10 ks.

The same results holds true also when we remove the 50% brightest pixels from the maps. It is not surprising that the ACFs obtained in this case give the same results as in the ideal map case (Fig. 3).

3.3.2 Galactic Foreground

Realistic DXB maps must account for the local contributions to the signal, i.e. for the Galactic foreground, which we model with two components: the Local Bubble and the Galactic Halo. The Local Bubble emission, generated by the hot gas within ~ 200 pc, is conveniently modeled as an unabsorbed thermal component with T $\sim 10^6$ K and solar metal abundances (Snowden et al. 1997; McCammon et al. 2002; Galeazzi et al. 2007; Gupta et al. 2009). In our maps it is included using the APEC model in the XSPEC package. The Galactic Halo, generated by thermal emission of gas within our Galaxy, is well described by an absorbed thermal component with T $\sim 2 \times 10^6$ K (Snowden et al. 1997; McCammon et al. 2002; Galeazzi et al. 2007). It is added to our maps by combining an APEC and a WABS model in XSPEC. Both models use the parameters listed in Tab. 3 of McCammon et al. (2002). The resulting SB of the Galactic foreground in the $380 - 650$ eV band is listed in Tab. 1. This galactic foreground model is effective since it matches the characteristics of the observed flux attributed to Galactic sources. Yet it is not accurate since it ignores the contribution from the Solar

Wind Charge Exchange (SWCX) which has been shown to outshine that of the Local Bubble (Koutroumpa et al. 2006, 2007; Henley & Shelton 2008; Gupta et al. 2009; Koutroumpa et al. 2009; Henley & Shelton 2010). The variable nature of the SWCX and the lack of strong observational constraints makes it difficult to model its contribution to the DXB. Fortunately, the very local origin of the SWCX excludes the presence of small (i.e $\theta < 10$') angular fluctuations so that its contribution to the Galactic foreground can be effectively modeled with an isotropic component which, following Gupta et al. (2009), we obtain by boosting up the contribution of the Local Bubble and Galactic Halo.

Since angular variations of the Galactic foreground are expected to be significant only on angular scales much larger that those relevant for our correlation study, we model it as a purely isotropic component that contributes a N_F photons in each pixel of the maps. For $t_{exp} = 1$ Ms, $N_F = 51.76$. Therefore, we obtain the number of Galactic foreground photons in the maps by Monte Carlo sampling a Poisson distribution with mean N_F.

The addition of the Galactic foreground significantly reduces the possibility of detecting the WHIM signature in the DXB in two ways. First, it decreases the amplitude of the ACF signal. According to Eq. 5 the expected decrement is $\sim 50\%$ in the case of $t_{exp} = 1$ Ms. The effect on the signal-to-noise error, however is less dramatic since the presence of a bright isotropic foreground greatly reduces the field-to-field scatter which dominates the noise. In fact, the overall reduction of the statistical significance of the correlation signal is just $\sim 20\%$. Second, and more serious, is the impact of the Galactic foreground on our capability of extracting the WHIM signal from the maps. The addition of a bright foreground outshines the correlation signal in the faint pixels. As a consequence, removing the brightest 50% pixels results in shot-noise dominated maps with zero ACF at all angles, as we have verified.

A simple solution to this problem is that of removing a model Galactic foreground before analyzing the ACF of the maps. Foreground removal would be then performed by simply subtracting the Galactic foreground model (a random counts map characterized by its mean intensity) to the photon count map. Since we assume that random counts are Poisson distributed, the subtraction is performed as follows. First we Monte Carlo generate the number of random counts in the pixel, F_{ij}. Then we compute the residual map $R_{ij} = T_{ij} - F_{ij}$ with the constraint that $R_{ij} = 0$ if $T_{ij} < F_{ij}$. Since this procedure removes less photons from the total map than those in the foreground map F_{ij}, we randomly remove the remaining photons from the pixels with $R_{ij} > 0$. Finally, we remove the 50% brightest pixels from this residual map. The result is displayed in Fig. 4. The panels show the same f.o.v. as Fig. 1. The extended, black areas correspond to the regions in which the 50% brightest pixels have been removed from the map. Isolated black pixels in the low-count regions are those with $R_{ij} = 0$.

This procedure to remove the foreground is very simplistic but, as shown in the top panel of Fig. 5 it is good enough to extract the WHIM autocorrelation signal from a $t_{exp} = 1$ Ms observation, since the ACF below $\theta \sim 3$' is significantly above zero and dominated by the WHIM component (red dashed curve).

As in the previous section, we do not add Poisson noise to the WHIM and *non*-WHIM counts. This choice is justified because, in addition to the fact that cosmic variance dominates over the Poisson noise of the signal for f $t_{exp} = 1$ Ms, as discussed previously, the Poisson noise is now dominated by the Foreground, not by the signal, which is included in our maps.

Given the uncertainties in the WHIM model adopted, these results are to be regarded as indicative. Yet, they serve to illustrate an important point: the capability of extracting the WHIM autocorrelation signal from the DXB maps is mainly hampered by the presence of a bright Galactic foreground. With this respect, our problem is analogous to that of extracting a weak signal in presence of a strong random noise. In this case, the signal-to-noise can be improved in two ways.

Since, in the large noise limit, signal-to-noise ratio scales as t_{exp}, the simplest option is to increase the exposure time. The effect of decreasing t_{exp} by a factor 10 is illustrated in the bottom panel of Fig. 5. In this case the ACF signal has been washed out everywhere but at sub-arcmin angular separations. Varying the exposure time should not affect the ACF signal but only its uncertainties, if they are dominated by Poisson noise. However, the two panels of Fig. 5 show that this is not the case. We have verified that this apparent inconsistency reflects a systematic bias introduced by our procedure to remove the foreground from a map in which the signal is dominated by the foreground itself. The shorter the exposure time, the less efficient the foreground removal, the more Poisson noise dominates the residual map. The net results is to wash out the ACF signal in the maps with shorter exposure times.

To assess the accuracy of our simple strategy to remove the foreground we have considered an additional procedure in which we remove a constant signal with amplitude equal to the mean foreground, but with no Poisson noise included, with the caution of avoiding negative photon counts. The results are basically the same as with the original procedure.

Rather then increasing the exposure time, a better alternative is to improve the map cleaning efficiency. First of all, one can perform a more effective exclusion of the *non*-WHIM signal by excluding (or filtering out) the signal in correspondence of known X-ray sources. Second of all, a better extraction of the WHIM signal can be obtained by convolving the map with Wiener-like filters (Wiener 1949; Press et al. 1992). Of course Wiener filtering relies on *a-priori* modeling of the WHIM ACF and Galactic foreground noise. However, possible inaccurate values of the Wiener Filter resulting from model uncertainties would introduce second order errors only (Rybicky & Press 1992).

Our analysis, therefore, clearly shows that long exposures are required to extract the WHIM autocorrelation signal from the ACF of the DXB. However, our considerations suggest that the value of $t_{exp} = 1$ Ms is probably too generous and that a significant detection might be possible with shorter exposures. This conclusion is corroborated by the recent results of Galeazzi et al. (2009), who studied the ACF of the DXB in a set of *XMM*-fields with t_{exp} ranging from 50 ks to 600 ks. After removing the contribution from known sources and making no attempt to subtract the Galactic foreground, they detect a positive autocorrelation signal in all fields (Fig. 2 of Galeazzi et al. 2009) that they interpret as the signature of the WHIM.

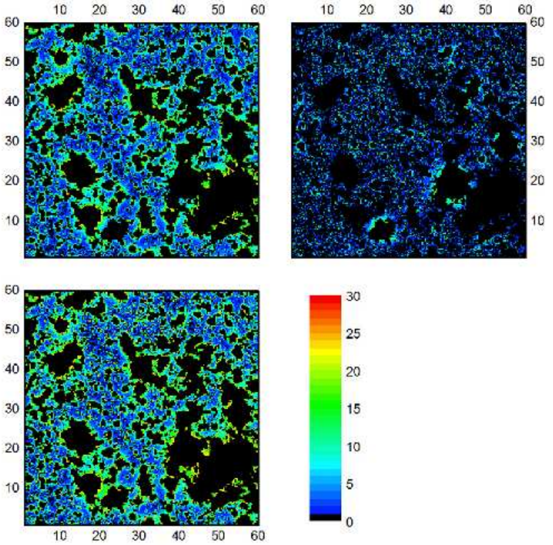

Figure 4. Residual maps of WHIM (*top-left*), *non*-WHIM (*top-right*), and *Total gas* (*bottom-left*) in the $380 - 650$ eV energy band for a f.o.v. of 1×1 deg^2, effective area of 1000 cm^2, and $t_{exp} = 1$ Ms. The color scale is in photon-number units.

Finally, we comment on the error contribution from the expected instrumental noise. The baseline of *Xenia* CCD detector is similar to that of *Suzaku* and relies on being placed on a low-Earth orbit. The rational behind this choice is to guarantee a more stable background than that in highly elliptical orbits where *Chandra* and *XMM-Newton* have been placed. The *Suzaku* instrumental background is $\sim 2 \times 10^{-5}$ counts kev^{-1} sec^{-1} mm^{-2} for XIS-FI and $\sim 5 \times 10^{-5}$ counts kev^{-1} sec^{-1} mm^{-2} for XIS-BI, i.e. 4 times and 9 times smaller than the cosmic X-ray background (Tawa et al. 2008). By comparison instrumental backgrounds for XMM-MOS and for XMM-PN are 2 times and 5 times smaller than the cosmic X-ray background.

3.3.3 Resolved and unresolved AGN

We also include the contribution of resolved and unresolved AGN in the mock maps.

Resolved AGN can be easily eliminated from the maps by excluding the contaminated pixels. However, given the limited number of expected objects, the effect is rather small. For $t_{exp} = 1$ Ms, *Xenia* is expected to resolve ~ 2000 AGN per square degree above the detection threshold S_{Xenia} of 10^{-16} erg cm^{-2} s^{-1} in the $0.5 - 2$ keV band (Piro et al. 2009). Under the somewhat simplistic assumption that each resolved AGN occupies just one pixel, the fraction of excluded pixels is just 3% of the total, much smaller than the 50% fraction of bright pixels that were excluded to remove the *non*-WHIM contribution. It is no surprise that removing this extra 3% of pixels has no appreciable impact on our result. It is also clear that a more sophisticated model, in which one account for the instrumental PSF, would not affect our results either. In fact the situation is even more favorable, since most of the AGN will be associated to massive structures contributing to the *non*-WHIM signal corresponding to the already removed 50% brightest pixels.

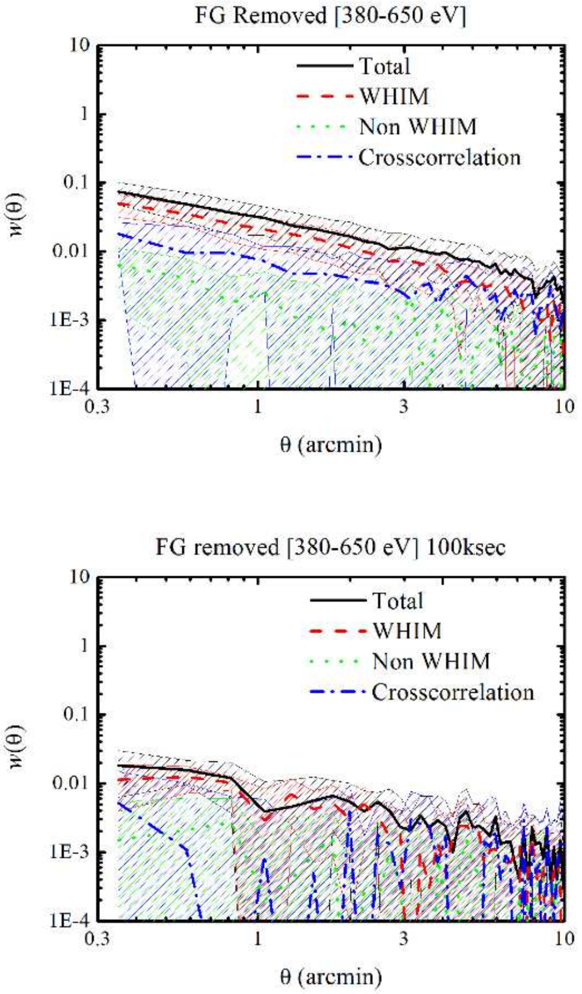

Figure 5. Comparison between the ACF of total map (*solid black*), WHIM component (*dashed red*), *non*-WHIM component (*dotted green*), and the cross-correlation (*dot-dashed blue*). All ACFs are normalized to the total flux after removing the brightest 50% of the pixels. The plots refer to the case of a $t_{exp} = 1$ Ms observation (*top*) and a $t_{exp} = 100$ ks observation (*bottom*).

To estimate the effect of unresolved object, we have included their contribution to the DXB by generating a population of unresolved sources matching the number counts and redshift distribution of faint AGN observed by *Chandra* and using N-body simulation to model their spatial correlation properties. More specifically, we generate a mock population of AGN as follows.

First we assume that mock AGN have the following number counts:

$$N(>S) \left\{ \begin{array}{ll} S^{-1.5}, & \propto S_{Lim} < S < S_{Chandra} \\ S^{-0.6}, & \propto S_{Chandra} < S < S_{Xenia} \end{array} \right. , \qquad (7)$$

where $S_{Chandra} = 3 \times 10^{-17}$ erg cm^{-2} s^{-1} is similar to the detection limit in the Chandra Deep Fields and $S_{Lim} = 6.5 \times 10^{-18}$ erg cm^{-2} s^{-1} is a lower limit so that the function does not diverge at infinity. In practice we require that mock AGN counts match the *Chandra* ones above S_{Lim} (Moretti et al. 2003) and assume that they follow the usual Euclidean slope below S_{Lim}. The reason of assuming a Euclidean slope rather than extrapolating the one of the resolved AGN is to maximize the contribution of unresolved objects to the DXB. To assign flux to the mock unresolved AGN we sampled the probability distribution obtained from Eq. 7 between S_{Xenia} to S_{Lim}. The total number of object is determined by requiring that unresolved AGN contribute to $\sim$ 12% of the Cosmic X-Ray Background (assuming a Cosmic X-Ray Background flux of 7.5×10^{-13} erg cm^{-2} s^{-1} deg^{-2} Moretti et al. 2003). In Tab. 1 we report the flux of the unresolved AGN in the $0.38-0.65$ keV energy band assuming a spectral slope $\Gamma = 1.4$. We end up by generating $\sim 5 \times 10^4$ objects per square degree with $S_{Lim} \leqslant S < S_{Xenia}$.

To determine the redshift distribution $\frac{dN}{dz}$ of these objects we integrate the AGN luminosity function of Hopkins et al. (2006) specified in three different redshift bins, out to $z = 3$.

Finally, we determine the spatial location of the mock AGN from the outputs of a collisionless N-body experiment under the assumption that AGN are located at the centre of dark matter halos. In practice, we extract 10 independent light-cones with f.o.v. of $1^\circ \times 1^\circ$ from the publicly available GIF simulations (Jenkins et al. 2001). Light cones are obtained by stacking all available outputs of the 479 Mpc h^{-1} computational cube out to $z = 3$. Within each cone we adopt a Monte Carlo rejection procedure to select a subsample of 5×10^4 dark matter halos with mass $> 1.4 \times 10^{12}$ M$_\odot$ h^{-1}, enforcing the required $\frac{dN}{dz}$. X-ray fluxes are randomly assigned according to Eq. 7 and the angular position of the AGN within each light-cone is obtained by projecting the spatial position of each selected halo on the $1^\circ \times 1^\circ$ f.o.v.

By construction, mock AGN have the same autocorrelation function of the dark matter halos, but no cross-correlation with the diffuse gas, since gas particles and dark matter halos have been taken from different simulations.

This inconsistency, however, is hardly an issue since, as we have verified, the angular autocorrelation function of the unresolved AGN is consistent with zero within the errors. We conclude that refining the AGN model to account for the spatial correlation with the gas distribution would not change our results. Unresolved AGN fainter than S$_{Lim}$ provide no significant correlation signal and can be regarded as an additional, weak isotropic signal to be added to the Galactic Foreground (Plionis et al. 2008).

Another potential class of sources that may contribute to the DXB is that of normal galaxies, thanks to their X-ray coronae and X-ray binary population. However, at the *Xenia* detection threshold for 1 Ms exposure, 10^{-16} erg cm^{-2} s^{-1}, their contribution is largely dominated by that of the AGN, as shown e.g. by Hickox & Markevitch (2006). To independently check the validity of this conclusion we have extrapolated the Log N/Log S of normal galaxies computed by Georgakakis et al. (2006) (Fig. 3 of their paper) down to $6.5 \times 10^{-18} - 1 \times 10^{-16}$ ergs s^{-1} cm^{-2} and computed their contribution to the diffuse background of *Xenia* . In this exercise we had to transform the original flux in the $[0.5 - 2]$ keV band into the X-ray band considered in this paper, $[0.380 - 0.650]$ keV. For this purpose we have assumed that the typical $0.380 - 0.650/0.5 - 2$ keV flux ratio for a normal galaxy is identical to that of the Milky Way. A choice that probably provides an upper limit since the the many Galactic lines that contribute to the flux in the $[0.380 - 0.650]$ keV are redshifted out of this range in the spectrum of a distant object. We find that the contribution of unresolved galaxies is 2.78×10^{-4} phot s^{-1} cm^{-2} sr^{-2}, i.e. a factor of ~ 2 smaller than that of the AGN. Had we assumed a more conservative, single power law $N(> S) \propto S^{-0.6}$ for the unresolved AGN, as e.g. in Hickox & Markevitch (2006), the relative contribution of normal galaxies would have been larger.

At lower fluxes the contribution of normal galaxies is expected to dominate over the AGN, but not over that of the WHIM, as discussed in Hickox & Markevitch (2007) and detailed in Table 1.

4 TRACING THE SPATIAL DISTRIBUTION OF THE WHIM

In this section we explore the possibility of performing 2D spectroscopy to characterize the 3D distribution of the WHIM. For this purpose we take the CRIS instrument as reference and use our mock 2D spectra to assess how well one can trace the 3D distribution of the WHIM using its characteristic O VII and O VIII emission lines. The angular and energy resolution of the instrument limits the ability of tracing the angular and redshift distribution of the WHIM, respectively. The exposure time determines the sampling density of the line-emitting gas. Here we consider the case of $t_{exp} = 1$ Ms.

The number of WHIM detections expected with an instrument like CRIS has been estimated by Takei et al. (2010). Their analysis shows that the minimum line surface brightness required for a 5σ detection is 0.07 photon cm^{-2} s^{-1} sr^{-1}and that the expected number of simultaneous O VII and O VIII detections is 639 per square degree, 426 of which are contributed by the WHIM (see Tab. 2 of Takei et al. 2010). In fact, the actual number of detections is expected to be significantly larger, since these estimates were obtained considering gas with $z < 0.5$, whereas the WHIM mass fraction is still large up to $z \sim 1$.

These detection estimates, however, have been obtained for an angular resolution ($2.6' \times 2.6'$) larger than that of our mock 2D spectra ($1.3' \times 1.3'$). As a consequence, we should revise detection estimates to account for the larger number of angular resolution elements available and for the larger threshold (0.22 photon cm^{-2} s^{-1} sr^{-1}) required for a 5σ detection. However, our goal is to detect line emitters that were obtained from a grouping procedure. It turns out that typical angular size of the emitters is closer to $2.6' \times 2.6'$ than to $1.3' \times 1.3'$ and we decide to keep the same threshold as Takei et al. (2010) to select detectable emitters. The fact that the number of detectable emitters is close to the estimates of Takei et al. (2010) confirms the goodness of this choice.

To characterize the spatial distribution of the line emitters we use the spatial two-point correlation function $\xi(r)$, which we compute using the same estimator used for the angular correlation function (see Section 3.1), generalized to the three dimensional case. The analysis is performed both in real and redshift space, i.e. by considering both comoving distances and "observed" redshifts. Finally, as already pointed out, since for our emitters the presence of a detectable O viii line often guarantees the simultaneous detection of the O vii line, in our analysis we will only consider O viii emitters.

4.1 Redshift distribution of line emitters

Before studying the spatial correlation properties of the O viii emitters, let us analyze their redshift distribution out to the comoving distance $d_c \simeq 1300$ Mpc h^{-1}, corresponding to the maximum redshift $z = 0.5$. In this redshift range the WHIM mass fraction is expected to increase by only $\sim 10\%$, whereas the mass fraction of the hot gas ($T > 10^7$ K) should increase by $\sim 50\%$ (Cen & Ostriker 2006). If O viii lines were mostly produced by hot gas in virialized structures we should observe a significant evolution in the number density of O viii emitters. On the contrary, if emission were dominated by the WHIM, the emitter number density should remain constant. Here we briefly remind the reader of the definition adopted in Section 2.1. The *Total Gas* consists of all gas with temperature above 10^5 K. The *Bright*-WHIM represents where the WHIM contributes to the X-ray emission is detectable (regardless of the non-WHIM). The WHIM-*dominated* gas consists of gas regions in which the WHIM contribution to the line emission is larger than that of all other phases.

Fig. 6 shows the cumulative density distribution of the O viii-line regions in the simulated light-cone as a function of the comoving distance d_c. Once we ignore the local region ($d_c < 300$ Mpc h^{-1}) dominated by a few structures and characterized by a large variance, we see that the comoving number density of all O viii emitters (green-dotted curve) is not too different from that of a volume limited sample, $N(< d_c) \propto d_c^3$ (blue dash-dotted). Deviations from this law exist for $d_c > 500$ Mpc h^{-1}. However, the fact that the slope of the *Bright*-WHIM curve (black, solid) is similar to that of the *Total Gas* suggests that they are not due to evolutionary effects. In fact, the similar shapes of the curves indicates that in both cases the emission is dominated by diffuse material, whose mass fraction hardly changes in this redshift interval, rather than by virialized gas. This result simply confirms that, due to the unfavorable ionization balance, the bulk of the O viii-line emitters does not trace the hot ($T > 10^7$ K) gas associated to galaxy clusters. Instead, they trace the gas located in the outskirts of virialized objects. Deviations from the $N(< d_c) \propto d_c^3$ curve simply derives from the fact that the volume of the resolution elements increases with the distance. This means that two nearby line-emitting regions along the same line of sight would be counted as two different emitters when they are close to the observer but would count as a single object at large distances.

The very fact that the cumulative number density of the WHIM-*dominated* (red, dashed) emitters decreases faster with the distance than that of the *Bright*-WHIM emitters corroborates this hypothesis. To understand this point, one has to keep in mind that the *Bright*-WHIM gas is found in the same regions, the outskirts of virialized objects, as the WHIM-*dominated*. The main difference is that the latter is, on average, considerably fainter, i.e. its lines are closer to the detection threshold. Therefore an extended region that looks like a single spot, if regarded as *Bright*-WHIM, would have a more patchy appearance when regarded as WHIM-*dominated* gas. The grouping procedure might then extract several WHIM-*dominated* emitters from a region in which only a single *Bright*-WHIM emitter is found. The magnitude of the oversampling decreases with the redshift as demonstrated by the fact that in Fig. 6 the total number of *Bright*-WHIM emitters matches that of the WHIM-*dominated* emitters at $d_c > 1000$ Mpc h^{-1}.

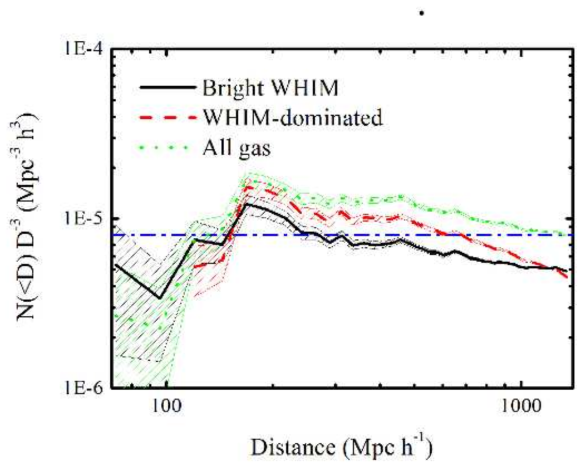

Figure 6. Cumulative distribution of O viii emitters normalized to that of a population of objects with constant number density $\propto d_c^3$. *Bright* WHIM (*solid, black*), WHIM-*dominated* (*red, dashed*) and *Total gas* (*green, dotted*) emitters. The *blue, dash-dotted* line is a reference distribution for a volume limited sample ($N(< d_c) \propto d_c^3$).

To summarize, the cumulative redshift distribution of the O viii emitters suggests little or no evolution in the range $z \in [0, 0.5]$. Deviations from a population of objects with constant number density and discrepancies between WHIM-*dominated* and *Bright*-WHIM emitters can be understood in terms of geometry effects. As fully explained in the following section, the errors shown in Fig. 6 are not estimated as scatter between different samples since we have only one catalog, instead we assumed a Poissonian distribution of emitters, and the errors are simply the square root of emitters' number.

4.2 Two-point correlation function in real space

Fig. 7 shows the spatial two-point correlation function, $\xi(r)$, of the detectable O viii-line emitters as a function of the comoving pair separation. The correlation function is measured in real space, ignoring peculiar velocities. The curves refer to the three families of emitters: *Bright* WHIM (black, solid), WHIM-*dominated* (red, dashed) and *Total gas* (green, dotted). The correlation functions are computed in comoving bins of 3 Mpc h^{-1} to account for the instrument energy resolution. Ideally, we would like to estimate errors from the scatter among the mocks, as in § 3. However, in this case we only have one mock catalog at our disposal. Fortunately, given the large volume covered by our mock 2D spectra and the limited number of detectable emitters, we expect that the errors in the $\xi(r)$ are dominated by sparse sampling rather than by field-to-field variance. To model shot noise we use Eq. 6, as we did in Section 3.3.1, this time adopting $N_R/N_D = 3$. In this work we rely on Eq. 6 rather than computing errors using more sophisticated techniques (bootstrap resampling, jackknife) since the main goal here is to obtain an order-of-magnitude estimate for the errors to assess our future capability of characterizing the correlation properties of the WHIM. In practice we will only trust differences that are significantly larger than the 1-σ width of the error-bands in Fig. 7

The main result of our analysis, shown in Fig. 7, is that O VIII emitters, whether or not contributed by the WHIM, are expected to be spatially correlated and their two point correlation function will be detected with high statistical significance by next generation experiments like *Xenia*. The large signal-to-noise ratio in the expected $\xi(r)$ demonstrates the robustness of this prediction which cannot be too much affected by uncertainties in the WHIM model and approximations in our error estimates.

All two-point correlation functions in Fig. 7 are well approximated by a power law with slope $\gamma = -1.7 \pm 0.1$ in the range $r = [4.5, 12]$ Mpc h^{-1}, steepening at larger separations. Such slope, determined via χ^2 minimization, is common to many cosmic structures, from galaxies to clusters and simply shows that both the O VIII emitters and virialized objects trace the underlying distribution of Dark Matter, as expected in a standard CDM scenario.

In particular, the correlation length of all detectable emitters (the *Total gas*) $r_0 = 4.0 \pm 0.1$ Mpc h^{-1} is consistent with that of optically selected galaxies as measured in several redshift catalogs (Zehavi et al. 2002; Hawkins et al. 2003). Such coincidence does not necessarily indicate a 1:1 relation between galaxies and O VIII emitters. Instead, it shows that both types of objects trace the same dark matter structures at separations > 3 Mpc h^{-1}, significantly larger than the virial radius of galaxy groups and clusters.

One interesting feature of Fig. 7 is that the correlation of the emitters contributed by the WHIM (*Bright*-WHIM and WHIM-*dominated*) is stronger than that of the *Total gas*, whose line emission is contributed by gas in groups and clusters. This result is counter-intuitive since hydro-simulations show that the WHIM preferentially traces the filamentary structure of the cosmic web whose spatial correlation is weaker than that of virialized objects. This results can be understood as the combination of two effects: a selection effect, derived from having imposed a given SB threshold, and the peak-biasing phenomenon (Kaiser 1984), which results from sampling the peaks of the underlying mass density field. In the case we are considering, the O VIII-line associated to the WHIM in filamentary structures is too weak to be detected. Only the WHIM in the outskirts of large, virialized structures is O VIII-bright enough to be detected. In other words: with our selection we only sample *Bright*-WHIM and WHIM-*dominated* emitters associated to galaxy clusters, whereas *Total gas* emitters are preferentially associated to the external regions of smaller, galaxy group-size structures. Galaxy clusters are associated to the highest peaks of the mass density fields, higher than those associated to galaxy groups. The higher the peaks, the larger their two-point correlation function (Kaiser 1984), which explains the stronger correlation of WHIM-contributed O VIII emitters.

We stress that the explanation above, though generally valid, has to be regarded as semi-quantitative since O VIII emitters are not directly associated to virialized structures, but to their outskirts, i.e. regions beyond their virial radius. For this reason it is not possible to interpret our result in terms of a halo biasing model, and infer the typical properties of dark matter halos from the correlation function of the O VIII emitters.

In Fig. 7 we also notice that the WHIM-*dominated* emitters are more correlated than the *Bright*-WHIM ones. The reason for this difference is more subtle. We have seen that both types of emitters sample the same regions (the outskirts of galaxy clusters) and so they should have the same correlation function. However, as we have discussed in Section 4.1, the WHIM-*dominated* emitters oversample these regions due to their patchy appearance. The result of oversampling the very same peaks of the density fields is to increase the correlation of the WHIM-*dominated* with respect to that of the *Bright*-WHIM emitters.

The small scale ($\leqslant 3$ Mpc h^{-1}) flattening of the correlation function is an artifact. It reflects the fact that the energy resolution of the instrument effectively acts as an anisotropic smoothing filter with radial scale of 3 Mpc h^{-1} which erases correlation on the corresponding scales. Once again, the different behavior of the WHIM-*dominated* emitters reflects their oversampling of the density peaks, which is particularly effective at small separations.

Fig. 7 shows the correlation function measured in the full light-cone. Since the mass fractions of different gas phases evolve differently we should check whether their correlation functions evolve in a different way too. To investigate this issue, we have measured the spatial correlation function of the O VIII emitters slicing the interval $z = [0, 0.5]$ into six bins. The results are shown in Fig. 8.

There is little evolution in the correlation properties of the emitters regions in the interval explored, with the exception of the nearest and outermost slices. At $z \sim 0.5$ the WHIM-*dominated* regions appear to be more correlated on larger scales than at lower redshifts. The simple explanation is, again, related to selection effect and peak biasing. At large redshift one detects stronger O VIII emitters associated to higher density peaks and the amplitude of the correlation function increases accordingly. On the opposite, at $z \sim 0$ all types of emitters are less correlated than at higher redshifts. The effect is particularly visible at large separations but its statistical significance is not large. The point is that the volume associated to the first slice of the cone is rather small and does not allow to fairly sample scales $\geqslant 10$ Mpc h^{-1}. Therefore, the error budget is likely to be dominated by cosmic variance rather than shot-noise errors. Adding the cosmic variance contribution would increase the size of the error-bands in Fig. 7 and reduce the statistical significance of the effect.

4.3 Correlation analysis in redshift space

From the analysis of the X-ray spectra one infers the 3D distribution of the O VIII emitters in redshift space, not in real space. The presence of peculiar velocity spoils the 1:1 relation between redshifts and comoving distances and introduces systematic distortions in the spatial clustering of the emitters and in their correlation properties. The net result is that the two-point correlation function measured in

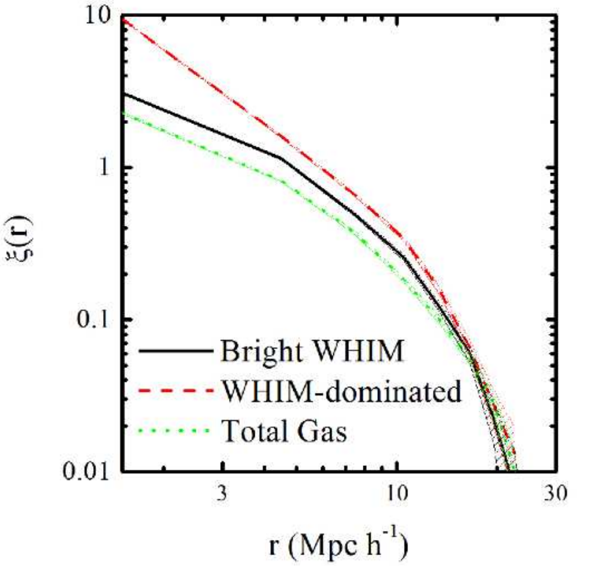

Figure 7. Real-space correlation function for *bright*-WHIM (*solid black*), WHIM-*dominated* (*dashed red*), and *Total gas* (*dotted green*) O VIII emitters. Shaded areas represent Poissonian uncertainties.

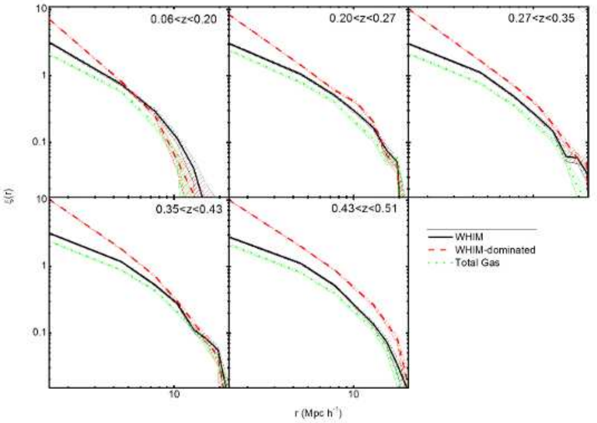

Figure 8. Real-space correlation function for *bright*-WHIM, (*solid black*), WHIM-*dominated* (*dashed red*), and *Total gas* (*dotted green*) O VIII emitters in six redshift slices. The redshift range is indicated in each panel.

redshift space is systematically different from the true one, measured in real space. The mismatch can be used to infer the properties of the peculiar velocity field, i.e. to characterize the dynamical state of the emitters.

Peculiar motions can be roughly divided in two categories. Incoherent motions, which typically dominate at small separations, and represent random velocities within virialized structures. They cause these structures to appear elongated along the line of sight in a characteristic type of distortion commonly known as “Fingers of God”. Coherent motions characterize large scale structures growing in the linear or quasi-linear regime and typically represent infall motions into mass overdense regions (or outflow from underdense regions). They apparently increase the density contrast associated to these regions along the line of sight.

For a collisionless fluid, like the galaxies in the universe, measuring these motions allows to infer important properties of the underlying mass density field: the amplitude of virial motions allows to infer the typical mass of virialized structures in the sample, while the size of coherent motions allows to constrain the growth rate of density fluctuations (Hamilton 1992; Guzzo et al. 2008) from which one can measure the mass density parameter Ω_m (Peacock et al. 2001) or test alternative gravity models (Linder 2005). For the case of a collisional dissipative fluid, like the O VIII emitting gas, one cannot derive these parameters from redshift distortions. However, it is still possible to infer the dynamical status of the gas which still brings some important information on the typical environment in which the WHIM is found. A strong Finger of God signature would indicate that the gas is preferentially found within virialized environments, while a dominance of the compression effect by coherent motions would indicate that the WHIM is preferentially found in regions of moderate overdensity moving toward virialized regions or outflowing from low density environments.

Peculiar velocities cause distortions only along the line of sight, and not on the transverse direction. One can therefore quantify their amplitude by comparing the clustering of objects in the directions parallel and perpendicular to the line of sight. For this purpose it is convenient to compute the two point correlation function after decomposing pair separations r into the line of sight component, π, and perpendicular to it, r_p. The resulting correlation function $\xi(r_p,\pi)$ is readily computed using the usual LS estimator. The three panels in Fig. 9 show the two-point correlation function $\xi(r_p,\pi)$ of the three types of O VIII emitters, projected onto the r_p,π plane. Different colors indicate different iso-correlation contours, whose amplitude is indicated in the color scale.

With no peculiar velocities, clustering properties are expected to be isotropic and iso-correlation contours would be circularly symmetric. Deviations from the circular symmetry would then indicate the presence of peculiar-velocity induced anisotropies in the spatial clustering of the emitters. The stronger the deviations, the larger the amplitude of peculiar velocities. As anticipated these distortions can roughly be divided in two categories. Incoherent velocities associated to Fingers of God type distortions cause the iso-correlation contours to be elongated along the π direction. Being associated to small-scale motions they constitute the dominant type of distortions at small values of r_p. Coherent motions associated to enhancements of density contrasts induce a compression of the iso-correlation contours along π. Since they are associated to large-scale motions, they dominate the distortion pattern at large values of r_p.

The iso-correlation contours shown in Fig. 9 display a non-negligible compression for $r_p \geqslant 6$ Mpc h^{-1} whose magnitude does not seem to depend on the type of emitter. This result suggests that on large enough scales, O VIII emitters trace the same underlying velocity field, characterized by linear, coherent flows, irrespective of their WHIM content. At smaller scales the iso-correlation contours appear to be elongated along the line of sight which characterize Fingers of God-type distortions. In fact, these distortions appear to be more prominent for WHIM-*dominated* emitters, while they seem to be absent in the *Total gas* case.

To make our analysis more quantitative and assess the statistical significance of these distortions, we have fitted the measured $\xi(r_p, \pi)$ with an analytic model that accounts for both large-scale coherent motions and small-scales by expanding $\xi(r_p, \pi)$ in Legendre polynomials out to the quadrupole term (Kaiser 1987; Hamilton 1992; Cabrè & Gaztañaga 2009). This model is fully characterized by two parameters: an "elongation" parameter σ_{12}, which quantifies the strength of Fingers of God-type distortions, and a "compression" parameter, β, which quantifies the strength of linear-type distortions. For a collisionless fluid, σ_{12} measures the typical strength of incoherent motions while β quantifies the amplitude of coherent motions, which is proportional to the growth of density fluctuations f: $\beta \propto f(\Omega_m) \propto \Omega_m^{0.55}$, where Ω_m is the mean mass density in units of critical density. For O VIII emitters such relations are not valid anymore. However, one can still measure σ_{12} and β, and compare them with the null case to detect the presence of either type of motions, or to compare the relative relevance of these motions among the different samples of O VIII emitters.

For this purpose we obtain the parameters β and σ_{12} by minimizing the χ^2-like function

$$\chi^2 = \frac{\sum_{ij}\left(y^m_{ij}(\beta, \sigma_{ij}) - y_{ji}\right)^2}{\epsilon^2_{ij}}, \tag{8}$$

where

$$y = log\left(1 + \xi(r_p, \pi)\right), \tag{9}$$

ϵ_{ij} is the Poisson error in the measured correlation function, the upper script m indicates the model and the sum runs over all bins (i, j) in which we have sampled the (r_p, π) plane.

The distortion model provides a poor fit at small perpendicular separation, as demonstrated by the fact that the reduced χ^2 decreases significantly when one excludes pairs with $r_p < 6$ Mpc h^{-1} from the analysis. This means that we cannot trust the value of σ_{12} obtained from the fit and therefore we cannot estimate the statistical significance of the Fingers of God-type distortions that appear more prominent in the WHIM-*dominated* emitters.

On the contrary, the model provides a good fit for $r_p > 6$ Mpc h^{-1} and the best fitting value of β appears to be robust since it does not change when including/excluding pairs with $r_p < 6$ Mpc h^{-1} from the fit or when we fix $\sigma_{12} = 0$. In Tab. 2 we list the best fit value of β and its 1-σ error for the three types of emitters considered. We only consider the case in which we exclude pairs with $r_p < 6$ Mpc h^{-1} since changing the cuts does not alter the result. For all types of emitters we measure a compression parameters β significantly above zero. This means that gas responsible for detectable O VIII lines is typically found in regions that are moving coherently toward large density concentrations, as expected for O VIII emitters that populate the outskirts of virialized structures rather than their central regions. Considering the approximation involved in our error analysis and the uncertainties in the models of WHIM, we do not regard the differences among the values of β for the different emitters as statistically significant.

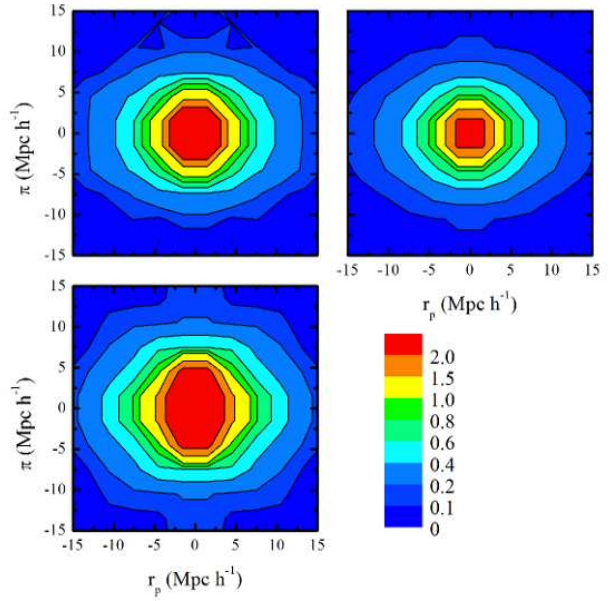

Figure 9. Iso-correlation contours for the measured two-point correlation function ξ in the plane (r_p, π) in redshift-space. The three panels refer to the three types of emitters considered. *Bright*-WHIM (*top-left*). *Total gas* (*top-right*). WHIM-*dominated* (*bottom-left*) The color scale quantifies the amplitude of the iso-correlation contours. (*bottom-right*).

Table 2. Best-fit values of the compression parameter β in the $\xi(r_p, \pi)$ at $r_p > 6$ Mpc h^{-1}

Emitter type	β
Bright WHIM	0.179 ± 0.023
Total gas	0.152 ± 0.018
WHIM-*dominated*	0.108 ± 0.022

5 DISCUSSION AND CONCLUSIONS

In this paper we have addressed two different, but tightly related, issues: the feasibility of indirect detection of the WHIM through the angular correlation analysis of the DXB and the study and characterization of the spatial distribution of the WHIM *already detected* through its O VIII X-ray line emission.

In this paper we have used the WHIM model described by Branchini et al. (2009) and Ursino et al. (2010) based on the hydrodynamical simulation of Borgani et al. (2004) with the metallicity-density relation taken from Cen & Ostriker (1999). Detectability and feasibility estimates assume next-generation X-ray satellite missions. As a reference case we have considered two instruments proposed in the framework of the proposed *Xenia* mission. For the angular correlation analysis of the DXB we have considered the HARI CCD-detector, while for the spatial correlation study we have considered the CRIS spectrometer.

The main results of our analysis can be summarized as follows:

- The DXB autocorrelation signal in the soft X-ray range [0.38-0.65] keV is mostly contributed by gas in hot and dense environments like clusters or groups. The WHIM contribution is comparatively smaller but significantly different from zero. However, the intrinsic correlation signals of the WHIM and *non*-WHIM are similar, implying that the different contributions to the ACF of the DXB reflect the different SBs of the two components. No unique feature in the ACF of the WHIM can be used to unambiguously infer its presence from the measured ACF. The zero-crossing of the WHIM ACF at $\sim 5'$ indicates the typical angular scale of the WHIM in emission and sets the minimum angular resolution required to next generation instruments aimed at detecting the WHIM in emission.
- According to our WHIM model, the *non*-WHIM signal originates from compact regions associated to virialized structures, while the fainter WHIM emission traces the outskirts of these regions. One can then hope to isolate the WHIM contribution by filtering out the signal associated to virialized structures, typically associated to the brightest spots in the maps. We found that the ACF measured after removing the 50% brightest pixels from the map is largely ($\sim 75\%$) contributed by the WHIM. More refined filtering procedures, in which one removes pixels associated to known objects, would certainly improve the results.
- The presence of an isotropic and comparatively brighter Galactic foreground component represents the main challenge to the WHIM indirect detection. We have found that a successful extraction of the WHIM ACF signal requires both an accurate modeling of the Galactic foreground and a long exposure time. The first requirement allows one to model the Galactic foreground as Poisson noise to be accounted for in the analysis. The second requirement allows to minimize shot noise errors. Our analysis suggests that exposure times of [0.1-1] Ms are required to measure the WHIM ACF. Uncertainties in the required exposure time generously allow for uncertainties in the WHIM model. Furthermore, it is possible to reduce the impact of the Galactic foreground studying the ACF at energies below $\sim$ 570 eV (the local O VII triplet). This means focusing at emission lines at redshift significantly different from zero, thus removing the strong contribution of the Galactic O VII and O VIII foreground (as partly done in Galeazzi et al. 2009).
- The AGN contribution to the ACF is small and easily removed by masking out pixels associated to resolved sources. In a deep ($\sim$ 1 Ms) exposure one expects to identify ~ 2000 AGN in a $1^\circ \times 1^\circ$ field. The corresponding fraction of removed pixels is a few % of the total. Unresolved AGN are basically uncorrelated and provides an isotropic contribution significantly smaller than that of the galactic foreground.
- O VIII emitters that can be detected in a 1 Ms observation show no density evolution in the range $z \in [0, 0.5]$. Deviations from the constant density case reflect the increasing volume of the resolution element with the redshift and the patchy appearance of the WHIM-*dominated* component.
- The two-point spatial correlation function of the O VIII emitters can be measured with high statistical significance out to separations of ~ 10 Mpc h^{-1}. Its amplitude and shape are close to those of optically selected galaxies, suggesting that both types of objects trace the same underlying mass distribution. O VIII emitters contributed by the WHIM are more correlated, as expected in the framework of the peak-biasing model since they are preferentially found in the outskirts of large virialized structures.
- The correlation properties of O VIII emitters do not significantly evolve in the interval $z \in [0, 0.5]$, despite the appreciable differential evolution in the mass fraction of the different gas phases.
- Anisotropies in the clustering of O VIII emitters induced by their peculiar velocities can be detected in the measured two-point correlation function and used to characterize their dynamical state. We have shown that the two-point correlation function of O VIII emitters detected after an observation of 1 Ms will allow to unambiguously detect such distortions which, according to our predictions, should be characteristic of infall motions toward virialized regions.

Our analysis indicates that next generation instruments will be able to detect the WHIM contribution to ACF of the DXB, but it will require a rather long exposure of $\sim$ 1 Ms. This prediction seems to be at variance with the recent results of Galeazzi et al. (2009) who found indirect evidence for a WHIM-like component in the angular correlation correlation properties of the DXB diffuse signal in several *XMM-Newton* fields with t_{exp} in the range [50-600] ks. As we argued in Section 3.3.2, the discrepancy is probably apparent since our predictions are to be regarded as conservative for two reasons. First of all, our model overestimates the SB of the *non*-WHIM components hence artificially increasing their contribution to the total ACF compared to that of the WHIM. Second of all, we use a very simplistic cleaning procedure that is not optimized to extract the WHIM signal. A better treatment of the *non*-WHIM component, capable of bringing theoretical prediction into agreement with currents DXB constraints, and a more effective cleaning procedure, that preferentially removes pixels associated to known objects, as Galeazzi et al. (2009) did, will significantly reduce exposure time required to perform the angular correlation analysis. With this respect the Galeazzi et al. (2009) results give us confidence that next generation instruments will be able to carry out a very effective observational campaign for the indirect search of the WHIM within a reasonably limited amount of time.

In fact, the comparison with Galeazzi et al. (2009) results constitutes a new observational test for our WHIM model. The ACF measured by Galeazzi et al. (2009) (their Fig. 1) is in agreement with the one predicted by our model (Fig. 5) for angular separations larger than $\theta = 2'$. At smaller separation the mismatch simply reflects the smoothing effect of the instrumental PSF which we did not try to model in our mock maps.

The fact that our WHIM model passes this further observational tests(the others being the O VI and O VII absorbers abundance and the DXB intensity) is certainly reassuring, but is no proof that our model is correct and its predictions robust. This concern, common to all WHIM models, has triggered a number of works aimed at testing the sensitivity of model predictions on crucial, ill-known processes of metal diffusion and stellar feedback (Bertone et al. 2010; Tornatore et al. 2010; Shen et al. 2010). Focusing on emission, we have seen that the main inconsistency of our model is the excess SB of the *non*-WHIM gas, whereas the soft X-ray emission of the WHIM meets the observational constraints. The natural question, then, is whether changing theoretical prescriptions for metal diffusion and galaxy feedback may help reducing the *non*-WHIM emission. One possibility is to invoke an AGN-driven rather than supernovae-driven feedback mechanism. Tornatore et al. (2010) found that, on average, AGN feedback increases the mass fraction and metallicity of the WHIM in regions with overdensities between a few and 10. However, the bulk of detectable WHIM emission is produced in regions with higher overdensity, in which AGN feedback decreases both the mass fraction and metallicity of the gas. The analysis of Bertone et al. (2010) is perhaps more relevant to us, since it focuses on the O VIII emission line. They show that detectability predictions are quite robust to the different model prescription with the exception of the cooling function. They show that using a metal-dependent cooling instead of a metal-independent scheme (as in our model) decreases by up to an order of magnitude the SB of the O VIII line in the bright areas ($SB \geqslant 1$ photon cm^{-2} s^{-1} sr^{-1}), dominated by *non*-WHIM emission, but does not significantly alter the SB of the fainter areas, largely contributed by WHIM emission. Then, on a qualitative level, the use of a metal-dependent cooling scheme, would help relieving the problem of our models.

Assessing, in a quantitative way, the impact of these results on the possibility of detecting and studying the WHIM is beyond the scope of this paper. Here we have simply estimated their effect by modifying our WHIM model in a way that effectively (but qualitatively!) mimics the impact of using a metal-dependent cooling scheme. For this purpose we have assumed an *ad-hoc* density-metallicity relation such that the metallicity of the gas with WHIM density remains unchanged, while it is decreased in high density region. We stress the fact that this is an *ad-hoc* model that only serves for illustrative purposes. The result of using this metallicity scheme is to decrease the mean SB in high density regions by $\sim 30\%$ while the one of the WHIM remains the same. The net effect is to reduce the SB contrast of the two phases although the relative statistics does not change appreciably, as indicated by the fact that in both the new and original metallicity schemes 50% of the pixels are dominated by WHIM emission. In terms of correlation analysis, the angular ACF of the WHIM remains the same but its statistical significance after the cleaning procedure increases significantly, as expected.

The results of this work and the robustness of the WHIM model predictions, suggest that a next-generation mission like *Xenia* will be capable of extracting and characterizing the WHIM contribution to the angular correlation properties DXB. We also expect to detect enough O VIII (and O VII) emitters to characterize the spatial correlation properties of the WHIM and its dynamical state. We confirm that, even with long exposure, next-generation instruments will only be capable of studying the spatial distribution of the WHIM in metal-rich, high density regions associated to the outskirts of large virialized structures, and of detecting the signature of its infall motion. Baryons tracing the large scale filaments of the cosmic web will remain largely undetected.

6 ACKNOWLEDGMENTS

We are grateful to Stefano Borgani for providing us the outputs of Borgani et al. (2004) hydrodynamical simulation realized using the IBM-SP4 machine at the "Consorzio Interuniversitario del Nord-Est per il Calcolo Elettronico" (CINECA), with CPU time assigned thanks to an INAF-CINECA grant. This work has been supported by contract ASI-INAF I/088/06/0 TH-018. Eugenio Ursino acknowledges financial contribution from contract ASI-INAF I/088/06/0 WP 15300.

REFERENCES

Bennett, C. L. et al., 2003, ApJS, 148, 97
Bertone, S., Schaye, J., Dalla Vecchia, C., Booth, C. M., Theuns, T., Wiersma R. P. C., 2010, MNRAS, 407, 544
Borgani, S. et al., 2004, MNRAS, 348, 1078
Buote, D. A., Zappacosta, L., Fang, T., Humphrey, P. J., Gastaldello, F., Tagliaferri, G., 2009, ApJ, 695, 1351
Branchini, E. et al., 2009, ApJ, 697, 328
Burles, S., Tytler, D., 1998, ApJ, 499, 699
Cabré, A., Gaztañaga, E., 2009, MNRAS, 393, 1183
Cen, R., Ostriker, J. P., 1999a, ApJ, 514, 1
Cen, R., Ostriker, J. P., 1999b, ApJ, 519, L109
Cen, R., Ostriker, J. P., 2006, ApJ, 650, 560
Cen, R., Fang, T., 2006, ApJ, 650, 573
Chen, X., Weinberg, D. H., Katz, N., Davé, R., 2003, ApJ, 594, 42
Croft, R. A. C., Di Matteo, T., Davé, R., Hernquist, L., Katz, N., Fardal, M. A., Weinberg, D. H., 2001, ApJ, 557, 67
Danforth, C. W., Shull, J. M., 2005, ApJ, 624, 555
Danforth, C. W., Shull, J. M., 2008, ApJ, 679, 194
Fang, T., Marshall, H. L., Lee, J. C., Davis, D. S., Canizares, C. R., 2002, ApJ, 572, L127
Fang, T., Canizares, C. R., Yao, Y., 2007, ApJ, 670, 992
Fang, T., Buote, D. A., Humphrey, P. J., Canizares, C. R., Zappacosta, L., Maiolino, R., Tagliaferri, G., Gastaldello, F., 2010, ApJ, 714, 1715
Fukugita, M., Hogan, C. J., Peebles, P. J. E., 1998, ApJ, 503, 518
Galeazzi, M., Gupta, A., Covey, K., Ursino, E., 2007, ApJ, 658, 1081
Galeazzi, M., Gupta, A., Ursino, E., 2009, ApJ, 695, 1127
Georgakakis, A. E., Chavushyan, V., Plionis, M., Georgantopoulos, I., Koulouridis, E., Leonidaki, I., Mercado, A., 2006, MNRAS, 367, 1017
Gupta, A., Galeazzi, M., 2009, ApJ, 702, 270
Gupta, A., Galeazzi, M., Koutroumpa, D., Smith, R., Lallement, R., 2009, ApJ, 707, 644
Guzzo, L., et al. 2008, Nature, 451, 541
Haardt, F., Madau, P., 1996, ApJ, 461,20
Hamilton, A. J. S., 1992, ApJ, 385, L5
Hartmann, D., et al., 2009, Astro 2010: The Astronomy and Astrophysics Decadal Survey, Science White Papers, no. 114

Hawkins, E., et al., 2003, MNRAS, 346, 78

Henley, D. B., Shelton, R. L., 2008, ApJ, 676, 335

Henley, D. B., Shelton, R. L., 2010, ApJS, 187, 388

Hickox, R. C., Markevitch, M., 2006, ApJ, 645, 95

Hickox, R. C., Markevitch, M., 2007, ApJ, 661, L117

Hopkins, P. F., Somerville, R. S., Hernquist, L., Cox, T. J., Robertson, B., Li, Y., 2006, ApJ, 652, 864

Jenkins, A., Frenk, C. S., White, S. D. M., Colberg, J. M., Cole, S., Evrard, A. E., Couchman, H. M. P., Yoshida, N., 2001, MNRAS, 321, 372

Kaastra, J.S., Werner, N., den Herder, J.W.A., Paerels, F. B. S., de Plaa, J., Rasmussen, A. P., de Vries, C. P., 2006, ApJ, 652, 189

Kaiser, N., 1984, ApJ, 284, L9

Kaiser, N., 1987, MNRAS, 227, 1

Kirkman, D., Tytler, D., Suzuki, N., O'Meara, J. M., Lubin, D., 2003, ApJS, 149,1

Klypin, A., Hoffman, Y., Kravtsov, A. V., Gottlöber, S., 2003, ApJ, 596, 19

Komatsu, E., et al. 2009, ApJS, 180, 330

Koutroumpa, D., Lallement, R., Kharchenko, V., Dalgarno, A., Pepino, R., Izmodenov, V., Quémerais, E., 2006, A&A, 460, 289

Koutroumpa, D., Acero, F., Lallement, R., Ballet, J., Kharchenko, V., 2007, A&A, 475, 901

Koutroumpa, D., Lallement, R., Raymond, J. C., Kharchenko, V., 2009, ApJ, 696, 1517

Kravtsov, A. V., Klypin, A., Hoffman, Y., 2002, ApJ, 571, 563

Landy, S. D., Szalay, A. S., 1993, ApJ, 412, 64L

Linder E. V., 2005, Phys. Rev. D, 72, 4

Mannucci, F., Bonnoli, G., Zappacosta, L., Maiolino, R., Pedani, M., 2007, A&A, 468, 807

McCammon, D., et al. 2002, ApJ, 576, 188

Moretti, A., Campana, S., Lazzati, D., Tagliaferri, G., 2003, ApJ, 588, 696

Morrison, R., McCammon, D., 1983, ApJ, 270, 119

Mushotzky, R. F., Cowie, L. L., Barger, A. J., Arnaud, K. A., 2000, Nature, 404, 459

Nicastro, F., et al., 2005, Nature, 433, 495

Tawa, N., et al., 2008, PASJ, 2008, 60, SP1, S11

Peacock, J. A., et al., 2001, Nature, 410, 169

Phillips, L. A., Cen, R., Ostriker, J. P., 2001, ApJ, 554, L9

Plionis, M., Rovilos, M., Basilakos, S., Georgantopoulos, I., Bauer, F., 2008, APJ, 674, L5

Piro, L., et al., 2009, ExA, 23, 67

Press, W. H., Teukolsky, S. A., Vetterling, W. T., Flannery, B. P., 1992, in *Numerical Recipes in C: The Art of Scientific Computing*, Cambridge University Press, New York

Rasmussen, A., Kahn, S. M., Paerels, F., den Herder, J. W., Kaastra, J., de Vries, C., 2007, ApJ, 656, 129

Rauch, M., et al., 1997, ApJ, 489, 7

Raymond, J. C., Smith, B. W. 1977, ApJS, 35, 419

Roncarelli, M., Moscardini, L., Tozzi, P., Borgani, S., Cheng, L. M., Diaferio, A., Dolag, K., Murante, G., 2006, MNRAS, 368, 74

Rybicky, G. B., Press, W.H., 1992, ApJ, 398, 169

Salpeter, E. E., 1955, ApJ, 121, 161

Shen, S., Wadsley, J., Stinson, G., 2010, MNRAS, in press Phys. Rep., 372, 1

Smith, B. D., Hallman, E. J., Shull, J. M., O'Shea, B. W., 2010, arXiv:1009.0261v1

Snowden, S. L., et al. 1997, ApJ, 485, 125

Spergel, D. N., et al. 2007, ApJS, 170, 377

Springel V., White M., Hernquist L., 2001, ApJ, 549, 681

Springel, V., Hernquist, L., 2003, MNRAS, 339, 289

Springel V., 2005, MNRAS, 364, 1105

Takei, Y., et al. 2010

Thom, C., Chen, H., 2008, ApJ, 683, 22

Tornatore, L., Borgani, S., Viel, M., Springel, V., 2010, MNRAS, 402, 1911

Tripp, T. M., Sembach, K. R., Bowen, D. V., Savage, B. D., Jenkins, E. B., Lehner, N., Richter, P., 2008, ApJS, 177, 39

Ursino, E., Galeazzi, M. 2006, ApJ, 652, 1085

Ursino, E., Roncarelli, M., Galeazzi, M., 2010, ApJ, 721, 46

Viel, M., Branchini, E., Cen, R., Matarrese, S., Mazzotta, P., Ostriker, J. P, 2003, MNRAS, 341, 792

Viel, M., Branchini, E., Cen, R., Ostriker, J. P., Matarrese, S., Mazzotta, P., Tully, B., 2005, MNRAS, 360, 1110

Weinberg, D. H., Miralda-Escudé, J., Hernquist, L., Katz, N., 1997, ApJ, 490, 564

Werner, N., Finoguenov, A., Kaastra, J. S., Simionescu, A., Dietrich, J. P., Vink, J., Böhringer, H., 2008, A&A, 482, L29

Wiener N., 1949, in *Extrapolation and Smoothing of Stationary Time Series*, Wiley, New York

Wiersma, R. P. C., Schaye, J., Smith, B. D., 2009, MNRAS, 393, 99

Wiersma, R. P. C., et al. 2009, MNRAS, 399, 574

Williams, R. J., Mulchaey, J. S., Kollmeier, J. A., Cox, T. J., 2010, arXiv:1008.5148v1

Yoshikawa, K., Yamasaki, N. Y., Suto, Y., Ohashi, T., Mitsuda, K., Tawara, Y., Furuzawa, A., 2003, PASJ, 55, 879

Yoshikawa, K., et al., 2004, PASJ, 56, 939

Zappacosta, L., Mannucci, F., Maiolino, R., Gilli, R., Ferrara, A., Finoguenov, A., Nagar, N. M., Axon, D. J., 2002, A&A, 394, 7

Zehavi, I., et al., 2002, ApJ, 571, 172